IEEE Access
Multidisciplinary | Rapid Review | Open Access Journal

Received December 6, 2019, accepted January 9, 2020, date of publication January 13, 2020, date of current version January 27, 2020.

Digital Object Identifier 10.1109/ACCESS.2020.2966241

Compact and Mobile Full-Field Optical Coherence Tomography Sensor for Subsurface Fingerprint Imaging

EGIDIJUS AUKSORIUS[1,2], KIRAN B. RAJA[3], BERKAY TOPCU[4], RAGHAVENDRA RAMACHANDRA[3], CHRISTOPH BUSCH[3], AND CLAUDE A. BOCCARA[1]

[1]Institut Langevin, ESPCI ParisTech, PSL Research University, CNRS UMR 7587, 75005 Paris, France
[2]Institute of Physical Chemistry, Polish Academy of Sciences, 01-224 Warsaw, Poland
[3]Norwegian Biometrics Laboratory, Norwegian University of Science and Technology, 2815 Gjøvik, Norway
[4]Tubitak Bilgem Uekae, 41470 Kocaeli, Turkey

Corresponding author: Egidijus Auksorius (egidijus.auksorius@gmail.com)

This work was supported by the EU-FP7 INGRESS Project under Grant SEC-2012-312792.

ABSTRACT Conventional fingerprint sensors that are deployed in real-life applications lack the ability to peer inside a finger beyond the external surface. Subsurface information can provide complimentary biometric characteristics associated with the finger. The subsurface fingerprints can also be employed when the quality of the external/surface fingerprints is affected. One of the most promising technologies for imaging below the surface of an external fingerprint is full-field optical coherent tomography (FF-OCT). However, the FF-OCT can be expensive and cumbersome, despite its proven ability for biometric use. In this paper, we describe the design and implementation of a compact, mobile and cost-effective FF-OCT sensor that is stable and easy to use. The newly designed sensor, being 30 cm $\times$ 30 cm $\times$ 10 cm in size, comprises of a dedicated silicon camera, stable Michelson interferometer and a bright Near-Infra-Red (NIR) light emitting diode. It enables recording of 1.7 $cm \times 1.7$ cm images of subsurface finger features, such as internal fingerprints and sweat ducts. We show the employability of the newly designed sensor for different applications. Specifically, we validate its usefulness by capturing subsurface fingerprints of 585 subjects leading to 3510 unique fingerprints. The resulting accuracy of 0.74% as Equal Error Rate (*EER*) indicates the backward compatibility of the proposed sensor with the existing commercial off-the-shelf algorithms. Thanks to the large fingerprint database collected in this work we determined the most useful imaging depth for the fingerprint matching purposes to be around 100 μm. As an additional advantage, the sensor could be readily used in other applications with little or no modification, such as *in vivo* skin imaging.

INDEX TERMS Biomedical imaging, biometrics, fingerprint recognition, full-field optical coherence tomography, microscopy, optical imaging.

I. INTRODUCTION

Fingerprint sensing is indispensable in many security oriented applications, such as access control to buildings and various devices, as well as border control [1]. However, current fingerprint imaging methods are sensitive to various surface artifacts, such as moisture, damage or dust. In addition, presentation attacks (aka., spoof attacks) are common where an artificial fingerprint can be used on top of a fingertip to gain access [2]. Therefore, there is an unmet need to develop more robust and secure fingerprint sensors, which would be able to record fingerprints more accurately and discriminate between *bonafide* (real) and artefact (fake).

A number of works have proposed innovative approaches to address this problem. One approach is to acquire three-dimensional information from within the fingers that would potentially provide additional information, such as in the 'multispectral fingerprint image acquisition' [3] or the capacitance-based fingerprint sensors in Apple iPhones. However, these are still largely surface-bound techniques as the penetration depth is quite limited - arguably around $10 - 50$ μm. Some important inner finger structures are much deeper than this [4], and therefore, a technology that is able to access that depth would be beneficial. For example,

The associate editor coordinating the review of this manuscript and approving it for publication was Chao Zuo.

a collection of skin layers, around $200-400\ \mu m$ beneath the finger surface, is composed of live cells that is collectively called the 'viable epidermis' or 'internal fingerprint' [5]. It essentially has the same topography as the finger surface, i.e., the top of the *stratum corneum*, and therefore, can in principle be used interchangeably with the surface fingerprint when the latter is damaged or otherwise not accessible due to factors such as external injuries, surgical alterations amongst many others.

An additional advantage of such an approach is that it is also capable of capturing the information of *sweat ducts* that is present in between the surface and the internal fingerprint. Capturing such sweat ducts can help not only to identify, but also to detect the presentation attacks (aka., spoofing attacks) [6]. Optical Coherence Tomography (OCT) has emerged as a promising new approach to capture such subsurface fingerprints [7], [8]. OCT can image through $1-2\ mm$ of biological tissue in a non-invasive manner making it suitable for forensics analysis of fingerprints [9]. While a confocal scanning OCT is currently offering the deepest imaging depth it is, however, expensive due to sophisticated laser technology and other components associated with running it. A viable alternative to the confocal scanning OCT is the less expensive OCT variant - Full-Field Optical Coherence Tomography (FF-OCT) [10], [11], which can use inexpensive light sources, such as Light Emitting Diodes (LED) or thermal sources, instead of the expensive lasers. FF-OCT also uses a camera that allows almost immediate fingerprint acquisition in contrast with the standard confocal scanning OCT which needs point-by-point image scanning to provide the so called *B-scan* - an axial image. The disadvantage of FF-OCT is somewhat lower imaging depth due to the absence of a pinhole used in the detection path of confocal OCT. Nevertheless, FF-OCT has been used with great success in many biomedical applications, such as, for example, imaging of skin [12], brain tissue [13], gastrointestinal wall [14] and cornea [15]. Other applications of FF-OCT include, for example, the detection of counterfeit currency notes [16]. Those applications exploited high resolution capabilities ($1\ \mu m$ in $3D$) but inherently had a small field-of-view (FOV). For fingerprint imaging we have to sacrifice the spatial resolution for a larger FOV necessary to capture enough of minutiae points for fingerprint recognition purposes.

Our first FF-OCT sensor for subsurface fingerprint imaging was built on an optical bench and was based on an expensive InGaAs camera and a cumbersome halogen bulb that was spectrally filtered at $1.3\ \mu m$ to provide $30\ nm$ bandwidth [17]. Recently, we have managed to decrease the price of the sensor by replacing the InGaAs camera with a silicon camera that was specifically designed for FF-OCT. It helped not only to decrease the price of the sensor but also improve the performance thanks to the superior camera specifications [18]. However, this FF-OCT sensor was still a benchtop system - too big and immobile for practical applications, such as field-tests. We, therefore, aimed here at miniaturizing the system and making it mobile. We expect that this sensor development would also lay grounds for enabling a more wide spread use of this technology. To this end, we report here on a detailed design and implementation of a compact, mobile and cost-effective FF-OCT fingerprint sensor. It was constructed to be robust, stable and easy to align, which is crucial for FF-OCT since it relies on low-coherence interferometry that is sensitive to various mechanical vibrations and misalignment.

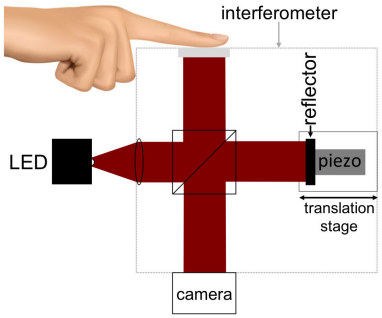

FIGURE 1. Simplified scheme of FF-OCT fingerprint sensor.

In order to validate the employability of the newly designed sensor, a large database was collected consisting of 585 subjects with 6 unique fingers per subject over two different sessions. The database, therefore, had 7020 fingerprint images with multiple (13) subsurface fingerprints recorded at different depths for each finger. A detailed analysis was further carried out to determine the biometric performance of the sensor and the obtained results are reported herewith.

In the rest of the paper, we discuss the design of the sensor in Section II and showcase various fingerprint imaging examples in Section III. Further, we present the details of the newly constructed FF-OCT fingerprint database and the verification performance analysis in Section IV.

II. FF-OCT SENSOR DESIGN

In this section, we present the design of the newly constructed FF-OCT sensor. The sensor was based on a powerful LED, an imaging Michelson interferometer and a dedicated silicon camera, as shown in Fig. 1. The detailed design is shown in Fig. 2, which was implemented on a $30\ cm \times 30\ cm$ optical breadboard. The complete system, displayed in Fig. 3, included a microcomputer, a screen and associated electronics. The focus of the design and the implementation was on making the sensor compact, lightweight, robust and easy to use for fingerprint imaging, which was important since the sensor had to be shipped for the field tests. We were trying to make all the elements, except the screen, small. Since we also tried to make the system cost-effective, we show the cost of the main components in Table 1.

The sensor was mostly built from the compact and light *Linos* optomechanical components with low optical axis height of $4\ cm$ above the breadboard. A lightweight slab of plexiglass of $30\ cm \times 30\ cm \times 1\ cm$ in size was used to cover the top of the system, as can be seen in Fig. 3, against which a hand could be rested during the fingerprint imaging for a more stable acquisition. A hole of $5\ cm$ in diameter

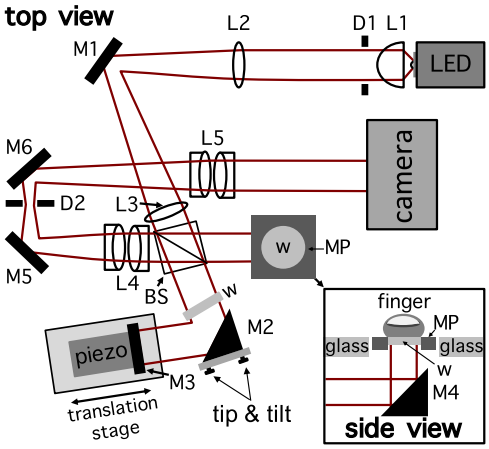

FIGURE 2. Detailed optical design and schematic (*top*−) view of the compact and mobile FF-OCT sensor. LED - Light emitting diode; *L*1 - aspheric collimation (collector) lens; *L*2 and *L*3 - singlet field and condenser lenses, respectively; *L*4 and *L*5 - objective and tube lenses, respectively, composed of two achromatic doublets in Plösl configuration; *D*1 and *D*2 - field and pupil apertures, respectively; *M*1 − 6 - mirrors/reflectors, *M*2 and *M*4 are cube mirrors. *M*2 is mounted on a tip and tilt stage for alignment purposes. Piezo-actuated weak reflector, *M*3 is mounted on a translation stage controlled by a stepper motor; *BS* - 50/50 beamsplitter; *w* - 5 *mm* thick antireflection coated window; *MP* - mounting plate (*Linos*). Inset shows a side view of a part of the system where a finger is put against a window for imaging. The window is mounted in the mounting plate. There is a plexiglass slab covering entire sensor area of 30 *cm* × 30 *cm* (only a part of it is seen in the side view). All three surfaces - the window, the mounting plate and the top glass are in one lateral plane.

FIGURE 3. A complete compact and mobile FF-OCT fingerprint sensor system that includes the sensor, the microcomputer and the screen (which was not optimized in terms of size).

was cut out in the glass so that it could be lowered on the top of the system, such that its surface would be at the same level as the window against which a finger is pressed for the measurements, as shown in the inset of Fig. 2 and is also seen in Fig. 3. The arrangement ensured that the whole hand could be in one plain and a finger does not have to be bent for imaging. The total height of the system was 10 *cm*, which included the breadboard and the glass support on the top. The overall sensor's height was limited by the height of the camera, which was 8 *cm*, but in principle can be further reduced if, for example, the camera is used without its cover. The FF-OCT sensor was mounted on 4 sorbothane feet of 2.7 *cm* height for vibration isolation since it was normally used on a regular office table without any vibration isolation during the fingerprint acquisitions.

TABLE 1. A list of main components (and their cost) used to build the sensor.

Component	Supplier	Model	Price, euros
Camera	Adimec	Q-2A750-CXP	9500
Frame grabber	Bitflow	Cyton-CXP4	2200
Microcomputer	Advantech	AIMC-2100-9S51	1350
Motor	Zaber	T-NA08A25	1000
Piezo actuator	Piezomechanik	HPSt 150/20	980
DAQ card	NI	USB-6000	170
LED + controller	Thorlabs	M850L3 + LEDD1B	506
Lenses	Thorlabs	Various	500
Mirrors	Thorlabs	Various	300
Beamsplitter	Thorlabs	BS014	207
Translation stage	Linos	G065114000	268
Mounting Plates	Linos	Various	500

A. OPTO-MECHANICAL DESIGN

As shown in Fig. 2, the illumination coming from the LED (M850L3, Thorlabs), which provided 900 mW of spatially incoherent light at 850 nm with the spectral bandwidth of 30 nm, was collimated with $f = 1.6$ cm aspheric lens $L1$. Light emitting chip of the LED (1 $mm \times 1$ mm in size) was magnified $\times 5$ by lenses $L1$ and ($f = 10$ cm) $L2$, so that the divergence of the emerging light from the LED is decreased. The design helped to retain as much of the LED's light as possible, which was necessary to operate the camera close to its saturation level. It also ensured the homogeneous illumination of the entire sample area that is imaged on the camera.

To implement the Köhler illumination, the image of the magnified chip was placed at the back focal plane of the condenser lens $L3$. The whole Köhler illumination system consisted of lenses $L1$, $L2$ and $L3$, and the field aperture $D1$. The aperture was adjusted such that there would be no light scatter in the sensor. The illumination was divided into the reference and sample arms by a non-polarizing beamsplitter with the equal splitting ratio of 50 : 50. A beamsplitter and the illumination arms were rotated in-plane by such an angle that the specular reflections from the beamsplitter's surfaces would be directed away from being detected by the camera.

Anti-reflection coated window of 5 mm- thick glass, mounted in a mounting plate (MP in Fig. 2), was used to press a finger against it. The contact provided stability and helped to flatten a finger out so that the whole image recorded by the camera would be filled with the fingerprint image. An identical window was inserted into the reference arm to match the dispersion between the two arms. A neutral density filter with 3 mm thickness and optical density of 6 was used as the reflector ($M3$ in Fig. 2) in the reference arm. The first surface of the reflector had reflectance of 4% at 850 nm, whereas light reflected from the second surface was suppressed by the absorption within the filter.

The reflector was mounted on a piezo actuator (HPSt 150/20 − 15/12, Piezomechanik) and the piezo-actuated reflector was placed on a compact Z-translation stage (*G*06511, *Linos*) equipped with an accurate and lightweight stepper motor ($T - NA08A25$, Zaber). The motor was effectively used to move the reflector on the micrometer scale and the piezo on the nanometer scale for phase modulation purposes. Another mirror ($M2$ in Fig. 2) in the reference arm was mounted on the tip and tilt stage for the alignment purposes.

Light coming back from the reference and the sample arms was recombined by the same beamsplitter and reimaged onto the camera with the objective and tube lenses ($L4$ and $L5$, respectively, in Fig. 2) in $4 - f$ configuration. It effectively performed $1 : 1$ imaging since the objective and the tube lenses had the same focal length of 10 *cm*. Each of the lens system contained a pair of achromatic doublets ($f = 20$ *cm*) arranged in the Plösl configuration (two lenses put together with the curved sides almost touching) for the better off-axis performance, which halved the effective focal length to 10 *cm*. Light coming back from the reference and sample arms interfered on the camera when the optical path length difference between the two paths was within the temporal coherence length of the light source.

B. DATA ACQUISITION

The most important and expensive element of the FF-OCT fingerprint sensor was the camera (Q-2A750-CXP, Adimec), which was specifically designed for FF-OCT. The camera was based on a unique CMOS sensor (CSI2100, CMOSIS) that had 2 Mega pixels (1440×1440), each 12 μm in size and capable of storing 2 millions of photoelectrons. Such a storing aptitude, called the Full Well Capacity (FWC), was achieved at the expense of increasing the read-out noise [19]. The noise, however, was still comparable to the shot noise when the camera was operated near its saturation limit, which is optimal operational condition for FF-OCT [11]. The camera could be run at the maximum speed of 720 frames per second (*fps*), which together with the large number of pixels and FWC put a high demand on the data transfer requirements between the camera and the computer. To address this, a PCI Express-based CoaXPress high-speed camera frame grabber (Cyton-CXP4, BitFlow) was used that was able to transfer the data at the maximum speed of 25 Gb/s. The sensor was controlled by a small (27.2 *cm* $\times$ 23.2 *cm* $\times$ 8.8 *cm*) but powerful microcomputer (AIMC-2100-9S51, Advantech) with one PCIex16 slot dedicated to the framegrabber.

C. DERIVATION OF FF-OCT IMAGES

FF-OCT images were derived from raw camera images, acquired with a phase shift between them that was imparted by the piezo in the reference arm. Subtracting such two recorded images one from another, computationally removes photons that come from other than a thin tissue slice defined by the temporal coherence length of the source (12 μm). Usually, four images are acquired for artifact-free reconstruction of the FF-OCT image by calculating $(I_1 - I_3)^2 + (I_2 - I_4)^2$, where I_n (with $n = 1, 2, 3, 4$) are the raw images with $\lambda/4$ path length difference imparted by the reference arm between the consecutive images. Unless otherwise stated, we averaged 50 raw images before performing the reconstruction of FF-OCT image, in order to improve the signal to noise ratio (*SNR*). The total acquisition time of a single FF-OCT image was therefore 285 *ms*. The microcomputer computed the FF-OCT images in real time alleviating image storing requirements. For subsurface fingerprint imaging on a large scale (database collection), 13 FF-OCT images were acquired at different depths by stepping the reference reflector every 50 μm between the acquisitions, resulting in images acquired in the range of 0 μm to 600 μm. Assuming the refractive index of the epithelium in finger was 1.42, the step size between the acquired images was then 35 μm and the axial range over which images were acquired in a finger extended from 0 μm to 420 μm below the surface. Acquisition of 13 subsurface images that took in total around 4 seconds was done in order to establish the most useful imaging depth for fingerprint recognition purposes. The subsequent analysis showed that employing only 3 subsurface fingerprint images acquired in the range of 100 μm - 170 μm results in the highest classification accuracy, shortening the effective acquisition time to 0.86 seconds.

D. SENSOR CONTROL

Sensor control and synchronization was carried out with a low-cost and lightweight data acquisition card (DAQ) (USB-6000, National Instruments), which generated a digital trigger signal for the camera, synchronized with the analog driving voltage for the piezo. The piezo driving voltage had to be amplified, by an in-house built amplifier since the power provided by the DAQ was too weak to generate $\lambda/4$ jumps every $\approx$ 1.4 *ms* (700 *Hz*), without considerable lag, necessary for the phase-shifting. Off-the-shelf components were used for the amplifier that consisted of a low-cost and high-speed operational amplifier (AD826ANZ, Analog Devices) powered by a power supply unit (PSU-203, Lascar).

E. SENSOR ALIGNMENT

Proper alignment and stability is critical in low-coherence interferometry since it relays on length of the sample and reference arms being matched on the micrometer scale. Also, light in the sample arm needs to be collinear with that of the reference arm in order to generate *enface* images - fingerprint images that extend across the whole field-of-view in one *enface* plane. Misalignments can appear because of the thermal drifts happening in the mechanical structure of the sensor. It can also appear because of deformations sustained during the sensor's transportation for the field tests. Therefore, the sensor might need to be realigned once after the transportation but it is quick and easy procedure. Micro misalignments in the sensor can also appear when a finger is put on the window for fingerprint acquisition. Such deformations are transient and cannot be corrected in real time but it can

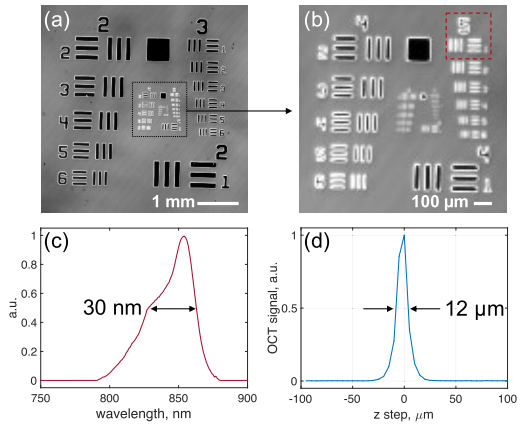

FIGURE 4. Measurements of the lateral and axial resolution. (a) Zoomed-in FF-OCT image of a resolution target indicating nearly aberration-free imaging. (b) Zoomed-in image of image (a) showing that the FF-OCT system is able to resolve a group of 15.3 μm bars (indicated with a dashed red box). (c) Spectrum of LED (measured by *Thorlabs*) that determines the temporal coherence length. (d) Measured optical sectioning curve.

affect image quality. Thus, every effort was made to ensure that the system is mechanically robust to such perturbations. To align (match) the arms in length, the reference mirror could be moved forwards or backwards by the Z-translation stage until the FF-OCT signal is detected. The signal comes from the surface of the window, against which a finger is pressed for imaging (the finger is not necessary during the alignment phase because the window reflects some of the light back from its surface despite the anti-reflection coating). If the signal is not spread across the entire image it means that the sample and the reference beams are not collinear. The beams could be brought back to the collinear configuration by adjusting a cube mirror in the reference arm ($M2$ in Fig. 2) that is mounted on the tip and tilt stage. The same adjustment is also used for setting the system to acquire an image of a fake and real fingerprint in one image, as explained below in Section III-B.

III. EMPIRICAL VALIDATION OF SENSOR AND ITS PERFORMANCE

A. SENSOR PERFORMANCE

The sensor could acquire 1.7×1.7 cm images with the spatial sampling rate of 2116 dots-per-inch (dpi). The numerical aperture (NA) was estimated to be 0.035 because of $f = 100$ mm objective lens and 7 mm pupil size (aperture $D2$ in Fig. 2). Thus, the estimated lateral resolution was 15 μm, as calculated from $0.61\lambda/NA$, for $\lambda = 850$ nm. To measure that experimentally, we have imaged USAF resolution target, shown zoomed-in in Fig. 4. There is no visible optical aberrations in Fig. 4(a) since the imaging system was highly corrected. As is evident in Fig. 4(b), the zoomed-in version of Fig. 4(a), bars of 15.3 μm in size (in element #1 of the group #5 shown in the dashed red box) can still be resolved, which effectively make it the sensor's lateral resolution. The camera was slightly undersampling spatially since it was sampling every 12 μm (size of the pixel) but the system's resolution of $15 - 16$ μm requires sampling with at least 8 μm, as per Nyquist requirement to avoid aliasing. However, that was not an issue here since, for example, for the fingerprint recognition purposes the spatial sampling rate of only 500 dpi (50 μm) is necessary, and therefore, pixels in fingerprint images are spatially averaged (binned) to increase SNR before feeding them to the matching algorithms. Also, opening pupil ($D2$ in Fig. 2) helped to detect more light that further increased SNR, and thus, allowed recording images with higher contrast below finger's surface. On the other hand, high spatial resolution achieved with the sensor allows imaging the so called $'level\ 3'$ features of the fingerprints [6], such as sweat ducts, as is demonstrated in this article in Fig. 6 and 7, which can also be used for the recognition purposes.

The depth of field (DOF) was estimated to be 1 mm (from λ/NA^2). Sufficiently large DOF was important since the imaging depth in finger was controlled by the reference reflector ($M3$ in Fig. 2) - moving the mirror enabled scanning finger axially, and thus, acquiring a stack. Since images are in focus only within the DOF it effectively determines the allowed axial scanning range. DOF of 1 mm allows to image all the subsurface finger features relevant for the identification, such as the *stratum corneum* and viable epidermis. Dermis-epidermis junction (DEJ) can also be imaged but with much lower contrast. Since viable epidermis is the most similar layer to the external fingerprint, imaging DEJ is not necessary, although that can be important in imaging various skin conditions for medical diagnostics purposes [20].

The spectrum of the LED, shown in Fig. 4(c), determines the coherence length of the light source, as defined by $0.44\lambda^2/\delta\lambda$. The bandwidth, $\delta\lambda$ of 30 nm results in 10.6 μm estimate of the coherence length, which is also termed the coherence gate in microscopy. The actual width of the coherence gate was measured by imaging a finger and analysing a small region in the FF-OCT images that was in contact with the window (ridge), and therefore, was acting as a mirror/reflector. The reference reflector was stepped every 5 μm in the range from - 0 μm to 600 μm with respect to the zero path delay difference condition. The derived curve is shown in Fig. 4(d) where the width of the curve is determined to be 12 μm - slightly larger than the estimate of 10.6 μm because of the non-Gaussian LED spectrum, as can be seen in Fig. 4(c). The axial resolution in finger could be estimated to be 8.5 μm, assuming the refractive index of epithelium is 1.42. The same data were used to estimate the sensor's sensitivity. The finger flattened by the window reflects $\approx$ 1% (20 dB attenuation), which is mostly due to the refractive index mismatch between the window and the finger. The sensitivity was estimated using the following expression: $-20log(\frac{I_{max}}{\sigma}) + 20dB$, where I_{max} is the signal amplitude recorded at the surface, σ - standard deviation of noise recorded at -100 μm and 20 dB accounts for the $\approx$ 1%

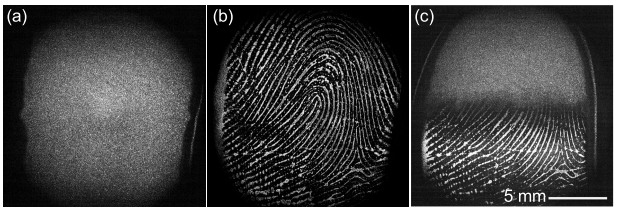

FIGURE 5. Imaging fingerprint through a scotch tape with FF-OCT sensor. (a) Image acquired 35 μm below the surface (inside the tape). (b) Image acquired 50 μm below the surface revealing the external fingerprint hidden behind the scotch tape. (c) Image acquired with the tilted reference mirror that allows capturing a part of the external fingerprint (bottom part) and the scotch tape (top part) in one image.

attenuation in the sample arm. The sensitivity was measured to be 88 *dB* when 50 images were averaged per phase, corresponding to the overall integration time of 0.286 *seconds*. To increase the sensitivity further the spatial averaging in the transverse plane or - in the case of 3*D* imaging - also in the axial direction, could be performed.

B. IMAGING OF FAKE FINGERPRINTS

Here we demonstrate that our sensor could be used to image a fingerprint when a finger is covered by a thin layer of scattering media, such as 50 μm-thick scotch tape. To record images, a finger with the tape on top of it was lowered onto the window (shown in the inset of Fig. 2). Fig. 5(a) shows an FF-OCT image acquired 35 μm below the surface, which only shows a structure inside the tape. At the depth of 50 μm we can see the external fingerprint, shown in Fig. 5(b). A clear fingerprint pattern is seen there despite the scotch tape absorbing and scattering the light. Fig. 5(c) shows an FF-OCT image that contains part of the tape and part of the fingerprint image, which was acquired by tilting the reflector in the reference arm ($M2$ in Fig. 2). The tip-and-tilt steering mirror introduced 0.3 deg tilt in the reference beam, which also effectively tilted the FF-OCT image by 0.3 deg from the *enface* condition. This ability to see multilayered structure in one image could be useful in certain situations. For example, a thickness of a particular layer could be calculated, just like in B-scan image provided by the scanning OCT. A tape like one used here can be utilized to, for example, hide a fingerprint from being imaged with the conventional FTIR sensor. It could also be used as a fake fingerprint if a different fingerprint is imprinted on the top of its surface. Thus, the sensor can be used for efficient presentation attack detection.

C. IMAGING OF SUBSURFACE FINGERPRINTS

The most important attribute of this sensor is its ability to acquire subsurface fingerprint features. To demonstrate this, a whole volume of a subsurface finger was recorded by capturing multiple *enface* images as a function of depths. The reference reflector was moved by 5 μm after each FF-OCT image, corresponding to 3.5 μm in the finger. Such sampling allowed to properly image entire finger's volume. Each FF-OCT image was recorded in 570 *milliseconds* since 100 images per single phase were averaged. Fig. 6 shows

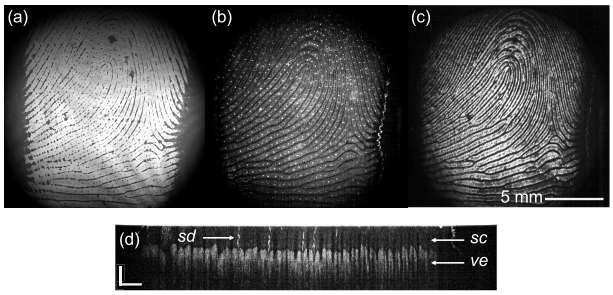

FIGURE 6. Fingerprint images (2116 *dpi*) acquired with the mobile FF-OCT fingerprint sensor at different depths. (a) An external fingerprint (0 μm below the surface). (b) FF-OCT image of the *stratum corneum* layer derived by integrating images in the range of 60 μm - 95 μm below the surface. Some sweat pores/ducts are visible. (c) FF-OCT image of viable epidermis (internal fingerprint) derived by integrating images in the range of 150 – 180 μm below the surface. (d) FF-OCT axial image (B-scan) of a finger. *SC* - the *stratum corneum*; *VE* - viable epidermis (internal fingerprint); *SD* - sweat ducts. The scale bar for (c) is 1 *mm* × 0.1 *mm* (*xz*).

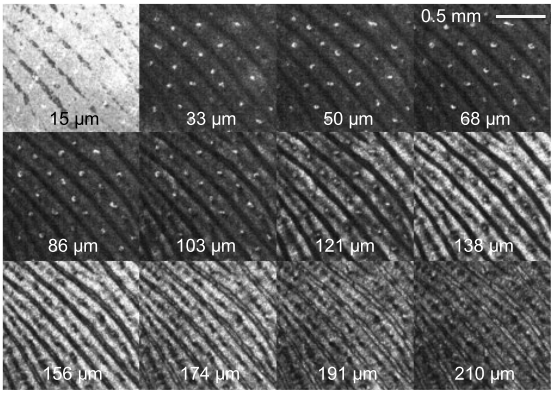

FIGURE 7. Small excerpts (1.38 *mm* × 1.38 *mm*) of subsurface fingerprints acquired with FF-OCT sensor at the progressively increasing depth with 2116 *dpi*. Images are displayed on a *log* scale. Image recorded at 15 μm is external fingerprint. Images shown in the range of 33 μm - 103 μm is the *stratum corneum*, with sweat ducts seen as white spots. Images shown in the range of 121 μm - 210 μm correspond to the viable epidermis. The images from 121 μm to 156 μm feature the ridges in the internal fingerprint, whereas images at the depth of 191 μm and 210 μm show the valleys of the internal fingerprint undergoing contrast inversion. The image depth was estimated assuming that the refractive index of epithelium is 1.42.

images (displayed at 2116 *dpi*) of external and internal fingerprints, as well as sweat ducts derived from the recorded volume. Fig. 6(a) shows an external fingerprint, which is equivalent to a fingerprint image generated with a standard fingerprint sensor, such as one based on the FTIR effect. Images in Fig. 6(b-c) were derived by averaging 10 subsequent images in the recorded stack. Fig. 6(d) shows an axial image, where various subsurface features, such as sweat ducts and the internal fingerprint, are clearly seen.

To better appreciate the high-resolution imaging capability of the sensor, we show zoomed-in images of different layers in Fig. 7 that were derived from the same data used for generating Fig. 6. The images contain high-resolution details, such as shapes of sweat ducts and its change with depth. One can also clearly see in Fig. 7, for example, that the sweat ducts stem from the middle of the internal fingerprint ridge, as is

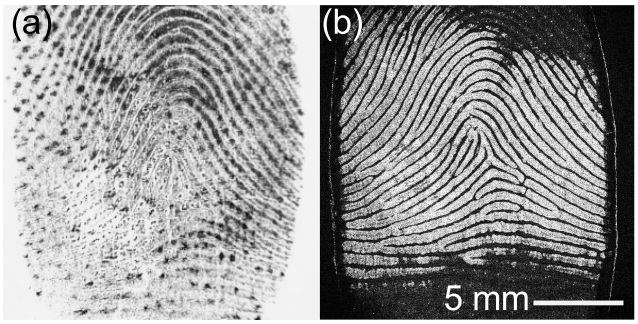

FIGURE 8. Imaging of a fingerprint damaged (abraded) with a sandpaper. (a) External fingerprint recorded with the standard commercially available fingerprint sensor (MSO 300, Morpho) that is based on the frustrated total internal reflection (FTIR). (b) Internal fingerprint image recorded with FF-OCT sensor.

evident in the images recorded at the depths of 121 μm and 138 μm for that particular finger.

D. IMAGING OF DAMAGED FINGERPRINTS

The FF-OCT sensor can be particularly useful when surface of the finger is heavily damaged. For instance, in the case where the epidermis may be eroded the internal fingerprint can still remain intact. Fig. 8 shows fingerprint images recorded with standard and FF-OCT sensors of a finger that was abraded with a sandpaper. Most of the epidermis has been removed from the finger surface. One can see that FF-OCT can still record a fingerprint image because of the remaining internal fingerprint, which is actually now easier to image because most of the scattering and absorbing epidermis layer is removed. This ability to image internal fingerprint can be useful in certain situation like, for example, when someone is trying to evade identification by destroying his/her external fingerprint (by rubbing against rough surface, such as wall, for example).

E. OTHER DESIGN CONSIDERATIONS

In this section we will discuss the reasoning behind the choice of this particular optical design with the imaging area of 1.7×1.7 *cm* and the sampling rate of 2116 *dpi*. One can argue that the imaging area could be expanded at the expense of lower sampling rate. For example, the imaging area of 7.2×7.2 *cm* can be obtained at 500 *dpi* potentially increasing the fingerprint matching performance. There were two main reasons why we have elected a smaller imaging area. The first was that imaging area of 7.2×7.2 *cm* would have resulted in much bigger and heavier sensor and would have required custom made optics. The second reason was that such high sampling rate of 2116 *dpi* allowed us to perform pixel binning in images when reducing them to 500 *dpi*. Pixel binning while downsizing increased contrast in subsurface FF-OCT images to a much greater extent than in conventional surface images, as explained below. In addition, such a design made the sensor a more versatile system since it could be used to image finger features close to the surface at the sampling rate of 2116 *dpi* enabling high-resolution imaging, as demonstrated in Fig. 7,

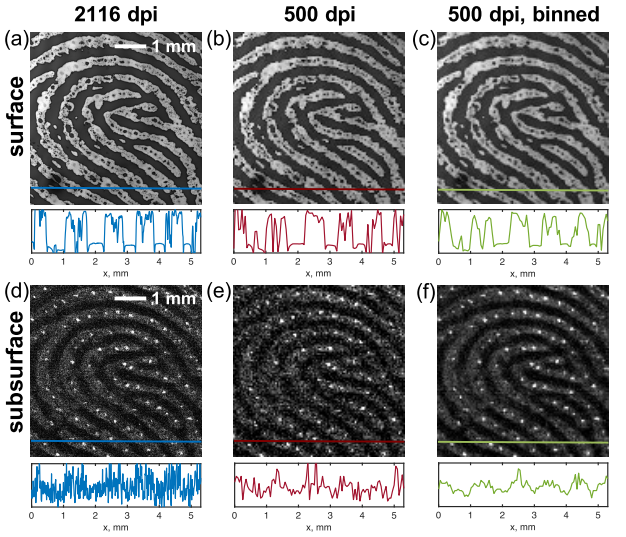

FIGURE 9. Excerpts (5.3 *mm* × 5.3 *mm*) of fingerprints demonstrating subsurface fingerprint contrast increase through *dpi* lowering (pixel binning). The contrast of the surface fingerprint (top) does not significantly change when the sampling rate is decreased from 2116 *dpi* (a) to 500 *dpi* (b and c). However, the contrast of the subsurface fingerprint (bottom) shows increase in the contrast when the sampling rate is decreased from 2116 *dpi* (d) to 500 *dpi* (f) by pixel binning (performing averaging when downsizing). The contrast change could also be seen in the line profiles shown below each image. Images (b) and (e) were derived by re-sampling (on average every 4.2 *pixels*) their high-sampling-rate equivalents (a) and (d), respectively. They do not show contrast change because they were not averaged when downsizing. Surface fingerprint (a) is the first layer in the acquired stack, corresponding to 0 μm below the surface. Subsurface fingerprint (d) is derived by summing up layers number 3, 4, 5 and 6 in the stack, that correspond to the depth range of 70 μm - 175 μm below the surface.

for example. In addition, lowering sampling rate down to the 500 *dpi* allows imaging deeper structures, such as internal fingerprints, with higher *SNR*. The sampling rate reduction down to 500 *dpi* by pixel binning helped to increase the subsurface FF-OCT image contrast and *SNR* by estimated factor of 18 (since on average 18 *pixels* were binned into one). We therefore pixel-binned all the images to 500 *dpi* that increased the contrast of subsurface images and fingerprint matching performance. To illustrate the effect of the binning on image contrast, Fig. 9(f) shows pixel-binned fingerprint image with 500 *dpi* derived from its full-resolution version (with 2116 *dpi*), shown in Fig. 9(d). The lines profiles shown below each image clearly indicate the contrast increase and noise decrease in the binned image. The surface (external) fingerprints, shown in Fig. 9(a-c), do not show significant image contrast variation with the sampling rate change, which is in contrast to the subsurface images. The surface images only appear more blurred as a result of binning because it leads to poorer spatial resolution.

The seeming insensitivity of image contrast to the sampling rate of the surface images can be explained by the relatively high signal coming from the finger surface. Such signal is not attenuated by the scattering or absorption in tissue, whereas subsurface images are greatly affected by it. Therefore, surface images acquired with FF-OCT are more like images acquired with the conventional fingerprint sensor based on

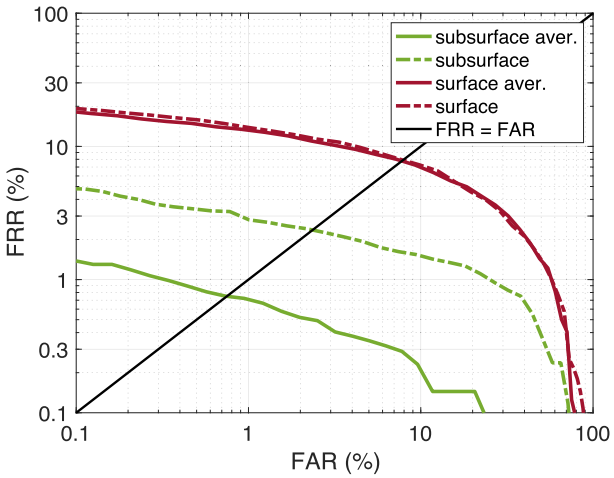

(a) DET curves - the False Rejection Rate (FRR) as a function of False Acceptance Rate (FAR) for surface (red curves) and subsurface (green curves) fingerprint images.

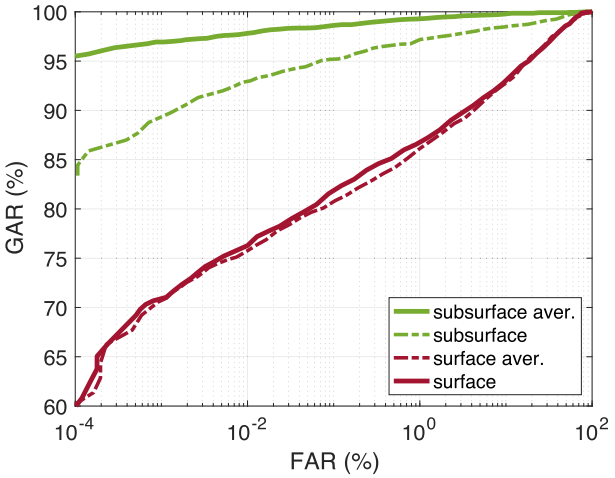

(b) ROC curves - the Genuine Acceptance Rate (GAR) as a function of False Acceptance Rate (FAR) for surface (red curves) and subsurface (green curves) fingerprint images.

FIGURE 10. ***DET*** **(a) and** ***ROC*** **(b) graphs derived for various biometric experiments. It demonstrates that binning (averaging while downsizing) increases matching performance and reduces the** ***EER*** **when using subsurface images. When pixel-binning (averaging) is performed during downsizing subsurface images to 500** ***dpi*****,** ***EER*** **of 0.74% can be achieved, as seen from green solid curve in (a). However,** ***EER*** **is 2.29% when no binning is performed, as seen from dash-dot green curve. Subsurface fingerprint images were derived by summing up 3 FF-OCT images acquired in the range of 105** μm **- 175** μm **(layer/image numbers 4, 5 and 6 in acquired stacks). The corresponding** ***DET*** **curves for surface fingerprints with and without averaging are nearly identical with** ***EER*** **equal to 7.6% and 7.8%, respectively, demonstrating that binning is less useful for surface-derived fingerprints.**

FTIR method, whereas subsurface FF-OCT images behave differently with the sampling rate change.

An argument that one can draw from the discussion above and from Fig. 9 is that expanding the imaging area to the extent that the sampling rate becomes 500 *dpi* would decrease the contrast of subsurface images since binning would be no longer possible, and thus, the *SNR* would be lower. Even though, the matching performance is generally increased with increased imaging area, however, it would be now partly offset by the decrease in the image quality (through lower *SNR*) in subsurface images acquired with FF-OCT. To demonstrate the binning effect on fingerprint matching performance we employed surface and subsurface FF-OCT images downsized to 500 *dpi* from 2116 *dpi*, with and without averaging (binning). The averaged and non-averaged subsurface images were of the same size (1.7×1.7 *cm*) but differed in the image contrast (or *SNR*), whereas surface images did not show contrast change, as shown in Fig. 9. Using the biometric analysis on large fingerprint database, described below in Section IV, we show in Fig. 10a that Equal Error Rate (*EER*) is lowered approximately 3 times when binning is performed on subsurface images and Failure To Enroll (FTE) - 22 times. Specifically, *EER* is reduced from 2.29% (dash-dot green curve) to 0.74% (solid green curve) when subsurface images are downsized to 500 *dpi* and *FTE* from 20.1% to 0.91%. The *EER* value for surface fingerprint FF-OCT images stays almost the same - 7.6% for averaged pixels (solid red curve) and 7.8% when no averaging is performed (dash-dot red curve). Meanwhile, *FTE* is reduced 2.6 times - from 12.3% to 4.6%. Since *EER* value is improved when pixel binning is available, the advantage of expanding the image area in FF-OCT sensor for imaging subsurface fingerprints is less obvious than in case of imaging the surface fingerprints for which *EER* does not show significant change.

Most importantly, however, the reason that we chose this particular design with the imaging area of 1.7×1.7 *cm* and the sampling rate of 2116 *dpi* was because we could use standard 1 *inch* optical elements, which significantly simplifies the sensor and the building process. Expanding the imaging area to 7.2×7.2 *cm* would not only require expanding the scan glass (w in Fig. 2) to this size but also about half of other optical elements in the sensor would have to be at least 7.2×7.2 *cm* in size, namely: the beamsplitter (*BS* in Fig. 2), lenses $L3$ and $L4$ and mirrors $M2$, $M3$ and $M4$ (all shown in Fig. 2). This would increase the overall sensor size and weight. For example, a 3-inch beamsplitter would weight 27 times more - 1.11 *kg* - than the 1 *inch* beamsplitter used here (41 *g*). Although lighter beamsplitters exist, such as pellicle or plate beamsplitters, however, pellicle beamsplitter of such size would result in significant stability issues because of its thickness (of a few micrometers only) and plate beamsplitter would have a problem of ghost reflections and would need another plate beamsplitter inserted in the sample arm for the dispersion compensation, which is essential in conventional FF-OCT. The bottom line is that it would require a new design and implementation of the sensor. Moreover, the new design would require nonstandard 3 *inch* optical elements that are not commercially available and would need to be custom made. Nevertheless, expanding the imaging area to 2 *inch* might be a good compromise since it would require 2 *inch* optical elements that are more conventional and commercially available. Such a sensor is planned to be built in the future.

The sensor would still be heavier and bigger than the sensor presented here but less compared to the one based on 3 *inch* elements.

IV. FF-OCT FINGERPRINT DATABASE AND PERFORMANCE

A. DATABASE COLLECTION

To demonstrate that such subsurface fingerprint images acquired with the FF-OCT sensor can be used for efficient biometric verification of individuals, a large database of fingerprint images was acquired at TUBITAK premises in Turkey. The FF-OCT sensor was shipped there and set for fingerprint recording. The database was captured from 585 subjects and 6 unique fingers of each person across two different session. The database thus consisted of 7020 fingerprint images along with the corresponding subsurface fingerprint images. Each of the 7020 acquisitions contained 13 FF-OCT images acquired at different depth (resulting in the total number of 91260 images). The depth was controlled by moving the reference reflector from 0 μm to 600 μm (which in finger corresponded to the depth range from 0 μm to 420 μm). The database was captured from subjects in a wide age range and almost equal gender ratio. The volunteers were asked to put a finger in the center of the window and press it slightly. Unlike the previous works where the data was captured from a set of people accustomed to non-hard labour [18], [21], in this work, the subjects were recruited from wider demographic and employment background. Further, the total number of subjects in the earlier works was only 20 [18], [21] while in this work, the number of subjects was 585.

B. BIOMETRIC ANALYSIS AND RESULTS

In order to empirically establish the applicability of the newly designed sensor and evaluate the backward compatibility of the fingerprint images captured using the sensor, we employed the commercial-off-the-shelf (*COTS*) fingerprint software from Neurotechnology, Lithuania. The choice of the *COTS* system was based on the *NIST* ranking for fingerprint verification where it was proven as one of the leading performers. Since the algorithms used for the minutiae extraction do not show accuracy improvement beyond the spatial sampling rate of 500 *dpi* we, therefore, reduced it from 2116 *dpi* to 500 *dpi*, which helped increasing the image contrast, as explained above. Various biometric experiments were carried out to find the best matching performance in terms of *EER*, that was derived from Detection Error Tradeoff (DET) curves, shown in Fig. 10a. To this end, different layers were included in the analysis. Specifically, images recorded at different depth were simply averaged and processed before the fingerprint matching analysis was performed. We found that summing up FF-OCT images acquired in the range of 105 μm - 175 μm (layer/image numbers 4, 5 and 6 in acquired stacks) gave the best matching performance - lowest *EER*, as described below.

As discussed earlier, the FF-OCT database consisted of 2 sessions, and therefore, we enrolled the images from the first session as reference/enrollment images while the second session was used as a probe set. Given that the FF-OCT database consisted of 585 users and 6 unique fingers for each subject, 32 of which were not enrolled due to the image quality, a total of 3478 genuine (mated) scores and 3487535 impostor (non-mated) scores were obtained. The resulting Detection Error Trade-off (*DET*) curve and Receiver Operating Characteristics (*ROC*) is depicted in Fig. 10. For example, it shows that the false rejection rate (*FRR*) was 1.38% at the False Acceptance Rate (*FAR*) of 0.1%. The corresponding *EER* was determined to be 0.74% from the *DET* curve, supporting the applicability of the new sensor for fingerprint imaging in real-life deployment. When compared to the matching performance obtained for the same set of people but carried out with a conventional fingerprint imaging device (MSO 300, Morpho), the *EER* value was determined to be lower - 0.12%. However, that is partly because processing of FF-OCT images is still not optimized due to the wealth of information that it offers and matching algorithms are optimised for conventional (surface) fingerprint images. Better algorithms need to be developed capturing more information that is being offered by this device. On the other hand, Fig. 11 shows that *EER* is higher for surface fingerprints and lower for subsurface ones. This could be explained by sub-optimal imaging window and some axial misalignment happening in some imaging experiments that generates artefacts in images. This will be addressed in the future version of the device. Fig. 11 shows *EER* as a function of the imaging depth (layer number). In other words, the graph shows the *'diagnostic'* value of each layer. One can see that FF-OCT image recorded at the depth of 105 μm has the most *'diagnostic'* value as it results in the lowest *EER* of 1.62%. This correspond to the reference mirror being translated 150 μm away from the zero

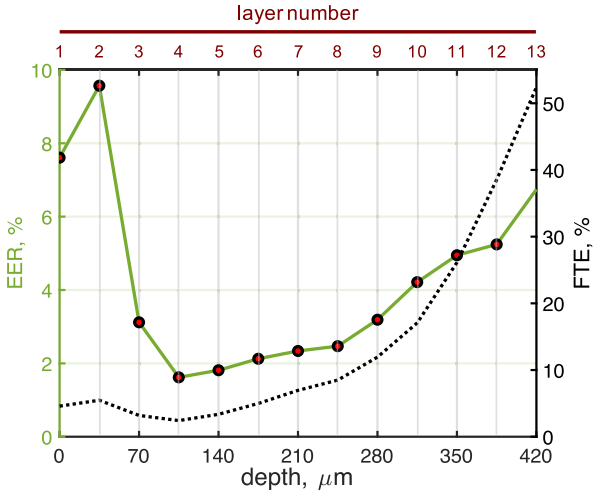

FIGURE 11. Equal Error Rate (*EER*) and Failure To Enroll (*FTE*) as a function of imaging depth (and layer number). *EER* (left *y* axis) is lowest when imaging at 105 μm. *FTE* (right *y* axis) follows similar trend as *EER* except for surface fingerprints where *FTE* is relatively low due to high signal. One layer corresponds to 35 μm. Layers number 4, 5 and 6 were included in the final matching performance analysis, shown in Fig. 10a that resulted in the *EER* value of 0.74%.

delay point. Fig. 11 also shows that *FTE* follows similar trend as *EER*, except for the surface part.

Apart from improving surface fingerprint images, a more optimum layer-averaging method is probably necessary to get better *EER*. To this end, we plan to use an image fusion approach that would also allow to include more layers in the analysis. Currently, the problem with it is that deeper layers invert contrast, as can be seen in Fig. 7 at 138 μm and 210 μm, for example. Summing such images together lowers the overall contrast and reduces the matching performance. Indeed, we found that summing image layers 4-8 (instead of layers 4-6) do not result in lower *EER*. Adding more layers actually start increasing *EER* - to 0.77% for layers 4-10 and to 1.1% for layers 4-12.

Ergonomic design of the FF-OCT sensor is not yet finalized. The conventional optical scanner, for example, has a finger guide that allows the subject to place his/her finger optimally, which FF-OCT sensor lacks. Finally, the conventional optical scanner has a built-in quality measurement step, rejecting images that are below an image quality threshold. This leads to a better enrollment with the optical device. All of those above points will be addressed in the future development of the FF-OCT sensor.

The question remains if it is better to record images at, say, the most '*diagnostic*' depth of 105 μm or acquire the same number of images from many different depth. To determine that, a new database would have to be collected where multiple images will be recorded at multiple depth. Fingerprint matching experiments can be then performed with various sets of images to determine the most optimal image acquisition procedure. The curves shown in Fig. 11 and the '*diagnostic*' depth of 105 μm is specific for FF-OCT and might be different for other OCT technique, such as scanning confocal OCT due to differences in multiply scattered light that is recorded.

V. CONCLUSION

In this paper, we have presented a new compact and mobile FF-OCT subsurface fingerprint sensor. Unlike the previous works, where the FF-OCT sensor was constructed on a bench top, the newly designed OCT sensor is mobile and cost-effective. The current sensor 30 $cm \times$ 30 $cm \times$ 10 cm in size can further be miniaturized with more compact design and smaller optomechanical elements. Using the sensor we have captured a large database of FF-OCT fingerprint images consisting of 585 subjects and resulting in 7120 unique fingerprint images. On the newly captured FF-OCT fingerprint database, the commercial-off-the-shelf fingerprint software resulted in an *EER* of 0.74% indicating the backward compatibility of the fingerprint images captured from the new sensor. The obtained accuracy also indicates the efficacy of the new sensor and its adaptability for real-life fingerprint imaging. In the future works, improvements in FF-OCT sensor shall be carried out, specifically, dark-field [22] and high-throughput [23], [24] configurations will be implemented to allow deeper/faster imaging, to obtain even better quality of the subsurface fingerprint images. Most importantly, algorithms will have to be developed for better extraction of subsurface information from FF-OCT images.

REFERENCES

[1] D. Maltoni, D. Maio, A. K. Jain, and S. Prabhakar, *Handbook of Fingerprint Recognition*. London, U.K.: Springer, 2009.

[2] C. Sousedik and C. Busch, "Presentation attack detection methods for fingerprint recognition systems: A survey," *IET Biometrics*, vol. 3, no. 4, pp. 219–233, Dec. 2014. [Online]. Available: https://ieeexplore.ieee.org/abstract/document/6985813

[3] R. K. Rowe, K. A. Nixon, and P. W. Butler, "Multispectral fingerprint image acquisition," in *Advances in Biometrics*. Springer, 2008, pp. 3–23.

[4] E. H. Holder, L. O. Robinson, and J. H. Laub, *The Fingerprint Sourcebook*. Washington, DC, USA: National Institute of Justice, 2011.

[5] A. Alex, B. Považay, B. Hofer, S. Popov, C. Glittenberg, S. Binder, and W. Drexler, "Multispectral *in vivo* three-dimensional optical coherence tomography of human skin," *J. Biomed. Opt.*, vol. 15, no. 2, 2010, Art. no. 026025.

[6] A. K. Jain, Y. Chen, and M. Demirkus, "Pores and ridges: High-resolution fingerprint matching using level 3 features," *IEEE Trans. Pattern Anal. Mach. Intell.*, vol. 29, no. 1, pp. 15–27, Jan. 2007.

[7] Y. Cheng and K. V. Larin, "*In vivo* two- and three-dimensional imaging of artificial and real fingerprints with optical coherence tomography," *IEEE Photon. Technol. Lett.*, vol. 19, no. 20, pp. 1634–1636, Oct. 15, 2007.

[8] A. Bossen, R. Lehmann, and C. Meier, "Internal fingerprint identification with optical coherence tomography," *IEEE Photon. Technol. Lett.*, vol. 22, no. 7, pp. 507–509, Apr. 1, 2010.

[9] M. Nioi, P. E. Napoli, S. M. Mayerson, M. Fossarello, and E. D'Aloja, "Optical coherence tomography in forensic sciences: A review of the literature," *Forensic Sci. Med. Pathol.*, vol. 15, no. 3, pp. 445–452, Sep. 2019.

[10] R. Leitgeb, "En face optical coherence tomography: A technology review," *Biomed. Opt. Express*, vol. 10, no. 5, pp. 2177–2201, 2019.

[11] A. Dubois, L. Vabre, A.-C. Boccara, and E. Beaurepaire, "High-resolution full-field optical coherence tomography with a Linnik microscope," *Appl. Opt.*, vol. 41, no. 4, p. 805, Feb. 2002.

[12] E. Dalimier and D. Salomon, "Full-field optical coherence tomography: A new technology for 3D high-resolution skin imaging," *Dermatology*, vol. 224, no. 1, pp. 84–92, 2012.

[13] O. Assayag, K. Grieve, B. Devaux, F. Harms, J. Pallud, F. Chretien, C. Boccara, and P. Varlet, "Imaging of non-tumorous and tumorous human brain tissues with full-field optical coherence tomography," *NeuroImage*, vol. 2, pp. 549–557, Jan. 2013.

[14] E. Coron, E. Auksorius, A. Pieretti, M. M. Mahé, L. Liu, C. Steiger, Y. Bromberg, B. Bouma, G. Tearney, M. Neunlist, and A. M. Goldstein, "Full-field optical coherence microscopy is a novel technique for imaging enteric ganglia in the gastrointestinal tract," *Neurogastroenterol. Motility*, vol. 24, no. 12, pp. e611–e621, Dec. 2012.

[15] V. Mazlin, P. Xiao, E. Dalimier, K. Grieve, K. Irsch, J.-A. Sahel, M. Fink, and A. C. Boccara, "*In vivo* high resolution human corneal imaging using full-field optical coherence tomography," *Biomed. Opt. Express*, vol. 9, no. 2, p. 557, Feb. 2018.

[16] W.-J. Choi, G.-H. Min, B.-H. Lee, J.-H. Eom, and J.-W. Kim, "Counterfeit detection using characterization of safety feature on banknote with full-field optical coherence tomography," *J. Opt. Soc. Korea*, vol. 14, no. 4, pp. 316–320, Dec. 2010.

[17] E. Auksorius and A. C. Boccara, "Fingerprint imaging from the inside of a finger with full-field optical coherence tomography," *Biomed. Opt. Express*, vol. 6, no. 11, p. 4465, Nov. 2015.

[18] E. Auksorius and A. C. Boccara, "Fast subsurface fingerprint imaging with full-field optical coherence tomography system equipped with a silicon camera," *J. Biomed. Opt.*, vol. 22, no. 9, Sep. 2017, Art. no. 096002.

[19] G. Meynants, X. Wu, S. Van Hoogenbemt, T. De Ridder, P. De Wit, K. Ruythooren, and K. Van Esbroeck, "700 frames/s 2 MPixel global shutter image sensor with 2 Me-full well charge and 12μm pixel pitch," in *Proc. IISW*, 2015, pp. 409–412.

[20] N. M. Israelsen, M. Maria, M. Mogensen, S. Bojesen, M. Jensen, M. Haedersdal, A. Podoleanu, and O. Bang, "The value of ultrahigh resolution OCT in dermatology–delineating the dermo-epidermal junction, capillaries in the dermal papillae and vellus hairs," *Biomed. Opt. Express*, vol. 9, no. 5, pp. 2240–2265, May 2018.

[21] K. B. Raja, E. Auksorius, R. Raghavendra, A. C. Boccara, and C. Busch, "Robust verification with subsurface fingerprint recognition using full field optical coherence tomography," in *Proc. IEEE Conf. Comput. Vis. Pattern Recognit. Workshops (CVPRW)*, Jul. 2017, pp. 144–152.
[22] E. Auksorius and A. Claude Boccara, "Dark-field full-field optical coherence tomography," *Opt. Lett.*, vol. 40, no. 14, p. 3272, Jul. 2015.
[23] E. Auksorius and A. C. Boccara, "Full-field interferential imaging systems and methods," U.S. Patent 16 320 982, Jun. 6, 2019.
[24] E. Auksorius and A. C. Boccara, "High-throughput dark-field full-field optical coherence tomography," *Opt. Lett.*, vol. 45, no. 2, p. 455, Jan. 2020.

EGIDIJUS AUKSORIUS received the Ph.D. degree in physics from Imperial College London for work on Fluorescence lifetime imaging and super-resolution STED microscopy. He subsequently worked as a Research Fellow with the Harvard Medical School and the Institute Langevin in Paris on high-resolution Optical Coherence Tomography (OCT) techniques. He is currently a Senior Researcher with the Polish Academy of Science. His current research interest includes the development and application of OCT to biomedical imaging.

KIRAN B. RAJA received the Bachelor of Engineering degree in electronics and communication from Visvesvaraya Technological University, India, in 2007, the M.S. degree from Erasmus Mundus Master CIMET, Saint-Étienne, France, and Gjøvik, Norway, in 2013, and the Ph.D. degree in computer science (image processing) from the Norwegian University of Science and Technology, Norway, in 2016. From 2007 to 2011, he was with Tata Elxsi Ltd., Bengaluru, India, Bally Technologies Ltd., Bengaluru, India, and Technicolor Inc., CA, USA. He is currently appointed as an Associate Professor with NTNU. His main research interests include statistical pattern recognition, image processing, and machine learning with applications to biometrics, and security and privacy protection. He has authored several articles in his field of interest and serves as a Reviewer for number of journals.

BERKAY TOPCU received the B.Sc. degree in telecommunications engineering, in 2007, and the M.Sc. and Ph.D. degrees in electronics engineering from Sabanci University, Istanbul, Turkey, in 2009 and 2016, respectively. He has been a Chief Researcher with the Biometrics R&D Lab, Tubitak Bilgem, Turkey, since 2010. His current researches include the areas of fingerprint verification and biometric template security. His research interests include biometrics, computer vision, surveillance, statistical signal, image processing, and pattern recognition. He has authored several articles in his field of interest and serves as a Reviewer for several international journals and conferences.

RAGHAVENDRA RAMACHANDRA received the bachelor's degree from the University of Mysore (UOM), Mysuru, India, the master's degree in electronics and communication from Visvesvaraya Technological University, Belgaum, India, and the Ph.D. degree in computer science and technology from the UOM and Institute Telecom, and Telecom Sudparis, Évry, France (carried out as a collaborative work). He was a Researcher with the Istituto Italiano di Tecnologia (IIT), Genoa, Italy. He is currently appointed as a Professor with the Norwegian Biometric Laboratory, Norwegian University of Science and Technology (NTNU), Gjøvik, Norway. He has authored several articles. He is also a Reviewer for several international conferences and journals. His main research interests include statistical pattern recognition, applied machine leaning, deep learning, data fusion schemes, and random optimization, with applications to biometrics, multimodal biometric fusion, human behavior analysis, and crowd behavior analysis.

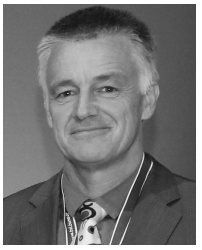

CHRISTOPH BUSCH received the Diploma degree from the Technical University of Darmstadt (TUD), Darmstadt, Germany, and the Ph.D. degree in computer graphics from TUD, in 1997. He joined the Fraunhofer Institute for Computer Graphics, Darmstadt, in 1997. He is currently a member of the Faculty of Computer Science and Media Technology, Norwegian University of Science and Technology (NTNU), Norway. He holds a joint appointment with the Faculty of Computer Science, Hochschule-Darmstadt. Further, he has been lecturing a course on biometric systems at DTU, Copenhagen, since 2007. His researches include pattern recognition, multimodal and mobile biometrics, and privacy enhancing technologies for biometric systems. He is the Co-Founder of the European Association for Biometrics and a Convener of WG3 in ISO/IEC JTC1 SC37 on Biometrics. He has coauthored over 400 technical articles. He has been a Speaker at international conferences. He served for various program committees. He is also an Appointed Member of the Editorial Board of the *IET Journal on Biometrics*.

CLAUDE A. BOCCARA received the Ph.D. degree in physical science from the UniversitÉ Paris-VI, in 1971. He is currently an Engineer with École supÉrieure d'optique, Paris, in 1965. He began his research work by studying dichroism with the Physics Laboratory of the ESPCI. He then worked at École Polytechnique and the University of California in Los Angeles. Among the optical methods, he has developed new microscopies to increase depth and lateral resolution. Recently, ultimate measurements have found new fields of application going from detection of gravitational waves to 3-D imaging though scattering media. He has published more than 300 scientific articles in international journals. In 2007, he founded the start-up LLTech devoted to medical imaging and diagnostics.